

Stress-strain distribution and failure mechanisms in dual-phase steels investigated with microstructure-based modeling

Labinot Topilla^a , Serkan Toros^{a*} 

^a Nigde Omer Halisdemir University, Mechanical Engineering Department, 51245, Nigde, Turkey. E-mail: labinot.topilla@gmail.com, serkantoros@ohu.edu.tr

*Corresponding author

<https://doi.org/10.1590/1679-78257157>

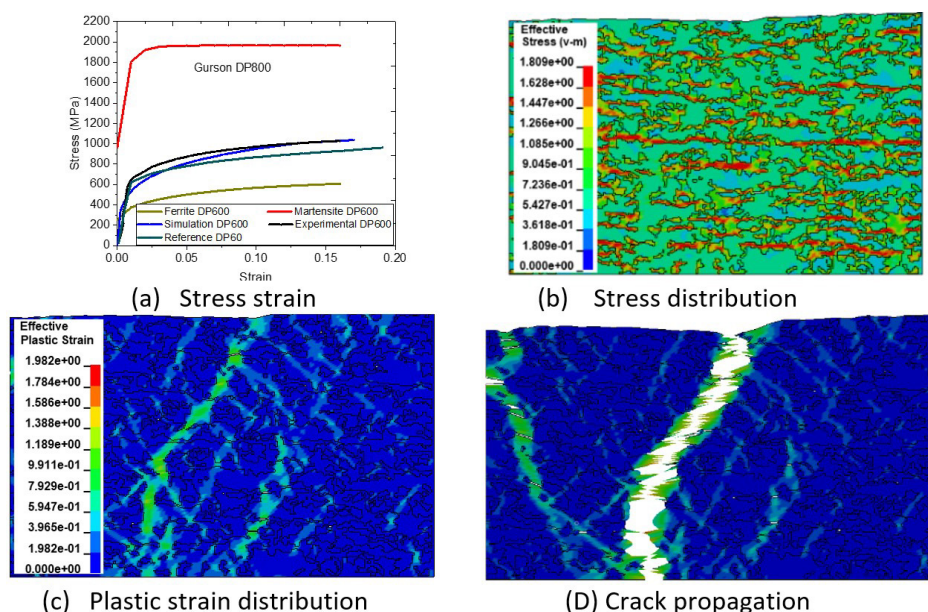
Abstract

In this study, the microstructural-based finite element modeling of dual-phase steels was investigated to visualize the crack initiation and its propagation through the phases that exist in the material. The parameters of various failure models, including Gurson, Gurson-Johnson-Cook, and Johnson-Cook (JC), were calibrated for different microstructure levels of DP600, DP800, and DP1000 steels. The onset of cracking, nucleation, void growth, and coalescence was determined using the models. As a result of the optimization studies, there is not much difference between the flow curves of the materials and the tensile values calculated from the tensile tests for DP600 and DP800, while it is slightly higher for DP1000. However, considering the fracture, martensite phases were found to be the main determinant of this situation. Cracks that start in the martensite phases then propagate through the ferrite phase and eventually cause the material to break. According to the results of the simulations, the difference between the experiments and the simulation results of the Gurson is 3.33%, the Gurson-JC is 1.82%, and the JC model is 2.39%.

Keywords

DP steels, 2D Microstructure, Plastic Strain, Stress Distribution Crack Propagation.

Graphical Abstract



Received June 15, 2022. In revised form October 16, 2022. Accepted October 20, 2022. Available online October 21, 2022.

<https://doi.org/10.1590/1679-78257157>



Latin American Journal of Solids and Structures. ISSN 1679-7825. Copyright © 2022. This is an Open Access article distributed under the terms of the [Creative Commons Attribution License](https://creativecommons.org/licenses/by/4.0/), which permits unrestricted use, distribution, and reproduction in any medium, provided the original work is properly cited.

Notations

ρ Density
 ν Poisson ratio
 σ_0 Flow stress of the material,
 $\dot{\epsilon}_r$ Strain rate
 ϵ_{N_1} Value is the strain when void nucleation happens
 S_{N_1} Standard deviation,
 f_N Volume fraction
 f Voids volume fraction
 f_c Critical void volume fraction
 f_f Fracture failure
 $q_1 - q_2$ Yield locus parameters
L1 Upper triaxiality factor
L2 Lower triaxiality facto
 $\bar{\epsilon}^p$ = Effective plastic strain
 σ^* The ratio of pressure divided by effective stress
 σ_h Hydrostatic stress
 $\dot{\epsilon}_M^{*pl}$ Effective plastic strain rate in the matrix
 σ_M Equivalent von Mises stress,
 θ Lode angle
 $\bar{\epsilon}^p$ Effective plastic strain
 $\Delta\epsilon^{pl}$ Is the increment in effective plastic strain
 σ Describes the flow stress,
 ϵ Equivalent plastic strain,
 σ_0 Considers the Peierls stress and the solid solution effect.
 α Constant
 μ Shear modulus
 b Burger's vector
 $d\alpha$ Ferrite and martensite grain size;
Mm Micron
 σ_y Yield Strangth
 σ_u Ultimate tensile strength
 $\Delta\sigma$ Strengthening by precipitation or the Carbon in solution for phases
Si Silicium
Cu Copper
Ni Nickel
Cr Chromium
Mn Manganese
C Carbon
P Phosphorus
K Hardening strength coefficient
M Taylor factor
E The elastic modulus
MPa Mega Pascal
A Initial yields strength
B Coefficient of strength
n Work hardening exponent
C Coefficient of strain rate
D1 , D2 , D3 and D4 J-C failure parameters
DP Dual Phase
GTN Gurson and Tvergaard and Needleman
ESP Effective plastic strain,
EPSO Effective plastic strain rate
MT Melt Temperature
ID: LCSS Load curve
FAIL Failure

RVE Representative volume element
RD Rolling Direction
G-JC Gurson Johnson Cook
FEM Finite Element Method
VP Viscoplastic
CP. Specific heat
OPT Optimization
EXP Experimental
JC Johnson Cook

1 INTRODUCTION

Dual-phase (DP) steels are the most widely used type of advanced high-strength steels (AHSS) in the automotive industry. The combination of high strength and formability improves passenger safety by increasing the energy absorption capacity and therefore crashworthiness. The microstructure of DP steels is composed of a ferrite matrix with embedded martensite islands (Ghadbeigi et al. 2013). One of the most significant challenges for the practical applications for these steels is related to the predictability of cracks. Therefore, Wu-rong et al., in (2011), In order to determine the largest blank diameter of SPFC340, DP600, DP800, and DP1000 with onset crack, this research first conducts limiting drawing ratio (LDR) studies. The four different types of blanks' fracture mechanisms are then compared and divided into two groups: necking crack and shear crack. Subsequently, the exact hardening formula for DP1000 was determined to match the flow curve derived from the elasticity test. The interconnected models were adapted to the Abaqus software and analyzed. The effects of the changes in patterns on the crack and spread properties of material cracks during the shear process were also determined. In addition, Rice and Tracey (1969) found the damage criterion to yield better results than those obtained using other examined criteria. Pickett et al. (2004) extensively studied the fracture time of materials with different damage criteria to determine the mechanisms of material breakage using various 'micro-mechanical models' such as: Gurson model, Gologanu model together with the Lemaitre mezo-scale damage mechanic's model. Moreover, the fatigue characteristics of Q420C steel welded joints and fatigue cracks were investigated experimentally based on the fracture morphology by Yang and Xing (2022).

Constant experimental and modeling efforts have been devoted by various researchers to identify the onset of local damage and deformation mechanism of high-strength advanced steel. Through experimental in-situ tensile testing using scanning electron microscopy (SEM) in conjunction with digital image correlation (DIC), the local deformation and damage mechanisms of commercial DP600 steel were investigated by Ghadbeigi et al. (2013). The correlation between the 1000 MPa DP steel microstructure and elongation obtained after the roll forming process was examined both microstructurally and micro mechanically by Ruiz-Andresa et al. (2015). The examination of the curved area using SEM showed changes in the ferrite-martensite microstructure. The plastic deformation of DP steels led to defects on the edges of the bent sheet, indicating that they contributed to the damage. In addition, electron backscatter diffraction (EBSD) measurements were performed for detailed characterization after rolling. A high degree of misorientation of the crystal lattice within the ferrite-strained grains was observed and was mainly concentrated in the ferrite/martensite grain boundaries. Investigations by Ramazani et al., (2013) using SEM and EBSD measurements revealed the changes in the microstructure of DP steel during deformation. Additionally, the material's two-dimensional (2D) microstructure was modeled, and the images of the material's current microstructure were compared to the model's results, determining that the experimental observations conformed well with the numerical results.

Several studies have examined the deformations of DP steels through various finite element (FE) computer programs. Therefore, FE simulations were performed in ABAQUS software by Paul (2013) used a representative volume element (RVE) and microstructure-based micromechanical model to investigate the deformation behavior, plastic strain localization, and plastic instability of DP 590 steel. Furthermore, Sirinakorn et al. (2014) determined the corresponding local stress-strain distributions to identify the critical strain for void nucleation on a micro/meso-scale by examining the deformation of DP1000 DP steel through the RVE method and ABAQUS software. In addition, they modeled the flow curve of single phases using the chemical composition of the phase. Moreover, the stress distributions, plastic equivalent strain, and crack propagation of DP600, DP800, and DP1000 steels were investigated through the finite element method by using COMSOL Multiphysics software in their works Çavuşoğlu et al. (2019). While, Zhou et al. (2015) investigated behavior of DP steel (980 MPa grade) through ABAQUS simulations, wherein microstructure images were used to simulate the micromechanical behavior. A sample microstructure image with a size of 110 μm to 110 μm or larger represents an RVE of this class of microstructures. Moreover, it was demonstrated that martensite carried the majority of the stress in this two-phase microstructure, whereas ferrites carried the majority of the strains.

de Geus et al. (2016) reported the comparison between the fracture initiation in the ductile soft phase and comparatively brittle hard phase of a DP material's microstructure. A simple microstructural model was used to predict the initiation of the macroscopic fractures. It was observed that only one of the phases dominated the macroscopic fracture initiation: the soft phase dominated with a low tension triaxiality, but above a critical triaxiality, the dominance of the hard phase was observed, leading to a strong decrease in the material's ductility. This transition depended heavily on the microstructural parameters. If the volume fraction of the hard phase was small, the break initiation was dominated by the soft phase even at a high phase contrast. At a high volume fraction of the hard phase, the hard phase dominated with a low phase contrast. Sodjit and Uthaisangskul (2012) investigated the impact of multiphase microstructure on the deformation behavior, wherein the DP microstructure was tested with different martensite phase fraction (MPF), and a subsequent 2D RVE model was created. The microstructure of the DP steels was spherical with irregular martensite and was different from that of a ferritic matrix.

In the present work, the deformation occurring in the standard plates at the microstructure level of the material has been determined through the representative volume element (RVE) method using finite element simulation. It is stated in the literature that due to the difficulties in determining the properties of individual phases. Crack propagation in ductile materials has not been studied enough by other studies through the finite element modeling method since nucleation and coalescence are difficult to model (Horstemeyer et al. 2003). Nevertheless, in this study, by using the proposed damage models, apparently successful crack initiation, nucleation, void growth, and coalescence processes were modeled.

However, research was also conducted using the finite element method to optimize specific parameters. The focus was on defining and calibrating the parameters of various failure models, such as nucleation parameters ϵ_N , S_N , and f_N , failure parameters f_c and f_f , and constitutive parameters q_1 - q_2 which belong to the Gurson_120_Mat model. Furthermore, previous Gurson parameters and damage parameters $D1$, $D2$, $D3$, and $D4$ which belong to the Gurson_johnson_Cook_120_Mat model, and finally, constitutive parameters A , B , n , and C , and damage parameters $D1$ - $D4$ which belong to the Johnson_Cook_098_Mat model. No previous studies have explored the crack propagation process and final fracture by finite element modeling simulations of the above-mentioned DP steels as extensively as the current study, using such unique models. And the most significant achievement of this study is the determination of damage parameters for the ferrite phase of the mentioned DP600, DP800, and DP1000 steels. Therefore, the effect of elongation on the granules of martensite and ferrite phases and the behavior of these phases at the microstructural level (even during the failure analysis) were investigated through an FEM study, and the obtained results are discussed at section 4.

2 MATERIALS AND METHODS

2.1 Experimental procedures

The primary focus of the present study is on numerical simulation; the experimental data for DP600 and DP800 were obtained from laboratory tests, while the data for DP1000 were extracted from a study by Çavuşoğlu et al. (2019). Briefly, the experimental uniaxial tensile tests of the abovementioned DP steels were performed at room temperature, with a strain rate of 0.16×10^{-1} , using a Shimadzu Autograph 100 kN tester machine. Tensile specimens were machined parallel to the rolling direction and in accordance with the ASTM E-8 standard, with gauge lengths of 50 mm, 12.5 mm in width, and 0.78 mm in thickness (Figure 1 (a)). And the mechanical properties of DP600, DP800, and DP1000 steels expressed through true stress-strain curves appear in Figure 1 (b). Their corresponding volume fraction, chemical composition and mechanical properties are listed in Tables 1-3.

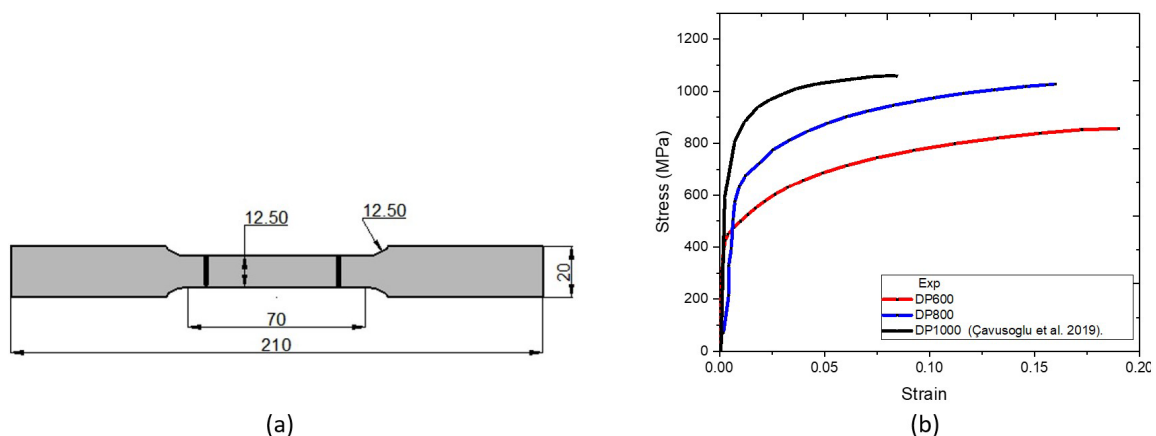


Figure 1. (a) Tensile specimen geometry, (b) True stress strain results of standard specimens

2.2 Microstructure analysis

In recent years, studies in computational materials science have become increasingly widespread. In this sense, not only macro-experiments but also micro-level evaluations and related simulation studies are becoming increasingly common in determining the behavior of materials under different conditions. Within the scope of the study, micro-level analysis was created in the examination of the mechanical behavior of 3 different commercial steels widely used in the automotive industry. These steels, which contain ferrite and martensite phases, where the hard martensite phase determines the strength of steel and the soft ferrite phase provides ductility (Çavuşoğlu et al. (2019), and Ghadbeigi et al. (2013)). The point to be noted here is that the strength property of the relevant material is directly related to the amount of % C at the martensite phase as, Katani et al. (2013) (see Figure 1 (b), and Table 1). Within the scope of this study, the phases were separated by using image processing techniques on the microstructure images, which had a 2D size of 125 × 93 μm obtained with the help of optical microscopes. When the figure is examined, the dark lines show the martensite phase and the light lines show the ferrite phase. Figure 2 The phases were separated with different sharp colors to determine the images more clearly Figure 3. In addition to the visualizations, a series of studies were carried out in order to determine the ratios of the phases in the relevant materials Table 1.

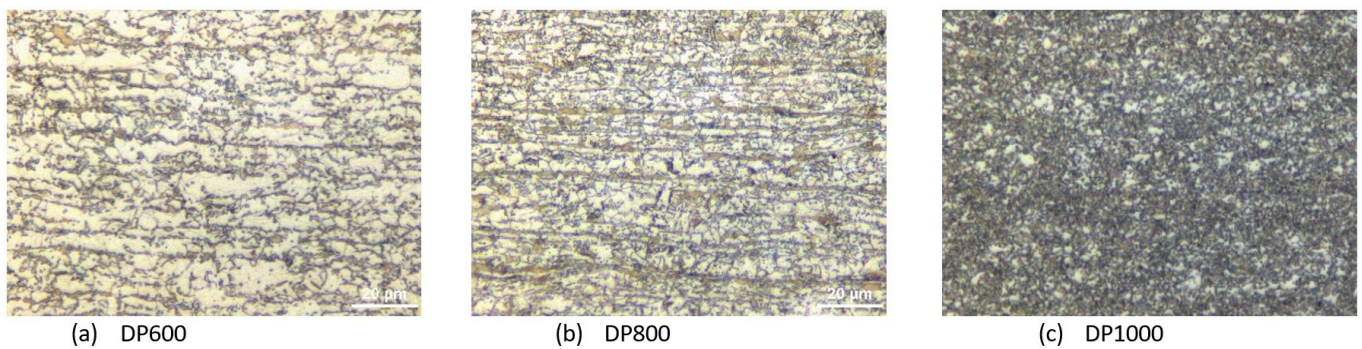


Figure 2. Micrographs of DP steels (bright phase ferrite, dark phase martensite).

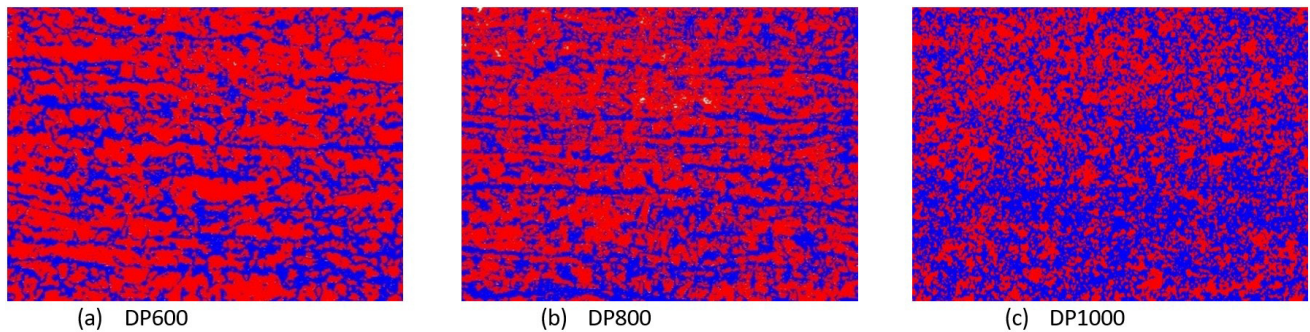


Figure 3. 2D representative volume element of DP steels.

Table 1. Ferrite and Martensite volume fraction of DP steels (%), Çavuşoğlu et al. (2019).

| Materials | Ferrite | Martensite |
|-----------|---------|------------|
| DP600 | 73.2 | 26.8 |
| DP800 | 66.8 | 33.2 |
| DP1000 | 52.5 | 47.5 |

2.3 Constitutive Description and Mechanical properties of DP600, DP800 and DP1000

In this study, a dislocation density-based strain hardening approach was applied to determine the flow curves in the ferrite and martensite phases (see Figure 4) according to the empirical relationship proposed by Rodrigues and Gutierrez (2003), as shown in equations 1 and 2.

$$\sigma = \sigma_0 + \Delta\sigma + \alpha \cdot M \cdot \mu \cdot \sqrt{b} \cdot \sqrt{\frac{1 - \exp(-M \cdot k \cdot \epsilon)}{k \cdot L}} \quad (1)$$

$$\sigma_0 = 77 + 750(\%P) + 60(\%Si) + 80(\%Cu) + 45(\%Ni) + 60(\%Cr) + 80(\%Mn) + 11(\%Mo) + 50(\%Nss) \quad (2)$$

All the values for each parameter for the constitutive description of a single phase are summarized in Table 3 and the descriptions of each term were given in the notation list. The concept of tables 2 and 3 is similar to the works tables of Li et al., (2019).

Table 2. Chemical composition of DP600, DP800, and DP1000 steels (wt-%), similar as Li et al., (2019).

| Steel | P | Si | Cu | Ni | Cr | Mn | C - Ferrite | C - Martensite |
|--------|-------|------|------|------|------|------|-------------|----------------|
| DP1000 | 0.015 | 0.1 | 0 | 0.03 | 0.48 | 1.4 | 0.008 | 0.45 |
| DP800 | 0.015 | 0.23 | 0.05 | 0.03 | 0.02 | 1.42 | 0.006 | 0.294 |
| DP600 | 0.015 | 0.1 | 0 | 0 | 0.48 | 1.58 | 0.006 | 0.234 |

Table 3. Parameters for the constitutive description of each single phase for DP600, DP800, and DP1000 steel, similar as Li et al., (2019).

| Steel | Phases | σ | σ_y | $\Delta\sigma$ | α | μ | M | b | k | L |
|--------|------------|----------|------------|----------------|----------|-------|---|---------|-------------|-------------|
| DP600 | Ferrite | 279.45 | 249.45 | 30 | 0.33 | 80000 | 3 | 2.5E-10 | 2.392344498 | 0.00 |
| | Martensite | 805.66 | 249.45 | 556.21 | 0.33 | 80000 | 3 | 2.5E-10 | 41 | 0.00 |
| DP800 | Ferrite | 252.2 | 222.2 | 30 | 0.33 | 80000 | 3 | 2.5E-10 | 3.333333333 | 0.000003 |
| | Martensite | 962.31 | 222.2 | 740.11 | 0.33 | 80000 | 3 | 2.5E-10 | 41 | 0.000000038 |
| DP1000 | Ferrite | 276.4 | 236.4 | 40 | 0.33 | 80000 | 3 | 2.5E-10 | 6.666666667 | 0.0000015 |
| | Martensite | 1454.65 | 236.4 | 1218.25 | 0.33 | 80000 | 3 | 2.5E-10 | 41 | 0.000000038 |

Moreover, the flow curves of the ferrite and martensite single phases calculated based on the model equations 1 and 2, and used parameters listed in Tables 2 and 3, are shown in Figure 4. Regarding the stress-strain curves of the phases, % C had the highest impact on strengthening in both the ferrite and martensite phases. Therefore, the 0.45% of C found in the phase martensite of DP1000 led to a flow curve with significantly higher stress compared to the martensite curves of DP800 and DP600. In contrast, the ferrite curves were highly suitable in terms of strengthening and stress (see Figure 4). Similar concept was emphasized after the works of Katani et al. (2013).

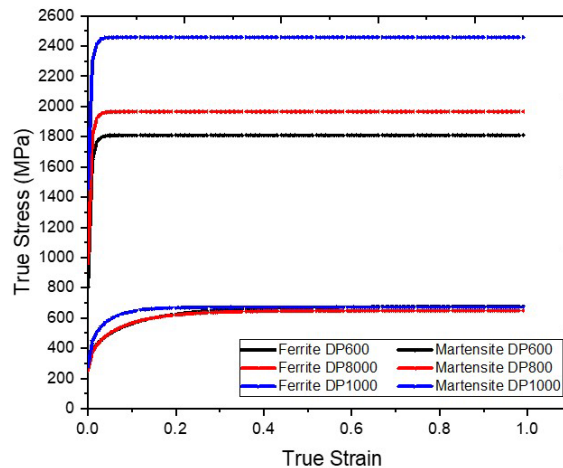


Figure 4. True stress strain curves for single ferrite and martensite phases corresponding to DP600, DP800, and DP1000 steels

3 FINITE ELEMENT MODELING MODELS

3.1 Gurson Model

Gurson model is dilatational-plastic model, which is integrated at LS-DYNA software and was used in this study. Below briefly was described the Gurson_120_Mat type, the extended explanations of the model can be found at (LS DYNA Maanual, 2012). The Gurson flow function is defined as follow equations 3 – 5 of reference Gurson (1977):

$$\Phi = \frac{\sigma_M^2}{\sigma_y^2} + 2q_1 f^* \cosh\left(\frac{3q_2 \sigma_H}{2\sigma_y}\right) - 1 - (q_1 f^*)^2 = 0 \tag{3}$$

The effective void volume fraction is defined as:

$$f^*(f) = \begin{cases} f & f \leq f_c \\ f_c + \frac{1/q_1 - f_c}{f_F - f_c} (f - f_c) & f > f_c \end{cases} \quad (4)$$

and the nucleation of new voids is defined as:

$$A = \frac{f_N}{S_N \sqrt{2\pi}} \exp\left(-\frac{1}{2} \left(\frac{\epsilon_p - \epsilon_N}{S_N}\right)^2\right) \quad (5)$$

3.2 Gurson–Johnson–Cook model

Gurson_JC_120_Mat is a model integrated into LS-DYNA software. Furthermore, this model consists of a combination of Gurson pressure dependent damage model with Johnson-Cook's triaxiality dependent failure criterion. The Johnson–Cook failure criterion was added to this material model and based on the triaxiality ratio, the σ_H/σ_M failure is calculated as equation 5. by including equations 3 - 6: (LS DYNA Maanual, 2012).

$\sigma_H/\sigma_M > L_1$: Gurson model

$L_1 \geq \sigma_H/\sigma_M \geq L_2$: Gurson model and Johnson-Cook failure criteria (5)

$\sigma_H/\sigma_M > L_2$: Gurson model

Johnson-Cook failure strain is defined as equation 6. (Johnson and Cook, 1985)

$$\epsilon_f = \left[D_1 + D_2 \exp\left(D_3 \frac{\sigma_H}{\sigma_M}\right) \right] (1 + D_4 \ln \epsilon) \Lambda \quad (6)$$

The meaning of the symbols is in the notation list. Λ is a function for including the mesh-size dependency.

3.3 Johnson–Cook model

In this study, the Simplified_Johnson_Cook_MAT_98 model developed independently of temperature, was used and the parameters of the hardening characteristic were determined through equation 6, (Johnson and Cook, 1983).

$$\sigma_y = (A + B\bar{\epsilon}^n)(1 + C \ln \bar{\epsilon}^*) \quad (7)$$

Further studies were carried out to determine the fracture level using Johnson_Cook_Mat_015 Model. The elongation at fracture of dual-phase steels were determined through equation 6 by defining parameters $D1-4$. The meaning of the symbols and a detailed description is in the notation list, and at (LS DYNA Maanual, 2012)

3.4 Micromechanics modeling of three different DP steels

After performing a 2D RVE modeling process by OOF2 software for mesh creation, the micrographs obtained from the DP steel "Abaqus style file created by OOF2" were imported to the LS-DYNA software, whereas in the axes of symmetry, the direction of deformation, and the failure parameters of deformation, were implied. Figure 5 shows the mash used and a schematic illustration of the symmetry axes and deformation directions used in the 2D RVE model. In the X direction, the deformations were applied until failure using the failure parameters of the applied models.

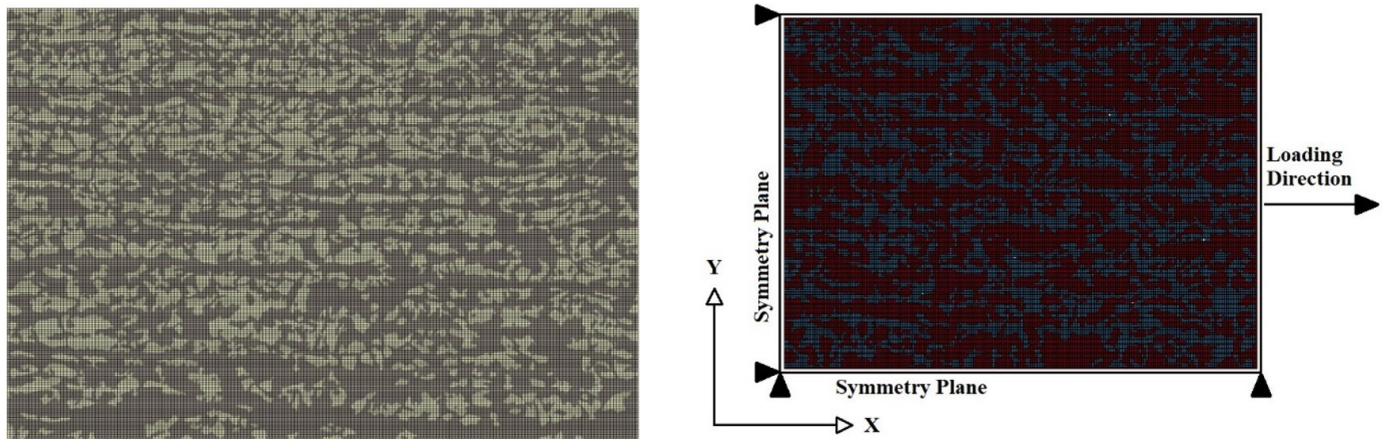


Figure 5. Mesh used and Schematic diagram of boundary conditions.

This research included three different types of AHSSs, namely, DP600, DP800, and DP1000 steels, and the investigations were performed using LS-DYNA software using three different destruction models: the MAT_GURSON_120 model, MAT_GURSON_JC_120 model, and the MAT_15_JOHNSON_COOK model. Two materials (MAT) were implemented in each card as we dealt with two phases, i.e., red phase ferrite and blue phase martensite (see Figure 6 finite element specimens used). In the nine cards, MAT_PIECEWISE_LINEAR_PLASTICITY_024 was used as the working material (MAT) for the martensite phase. The respective strength martensite flow curves of Figure 4 were used for all the three steels investigated, and the failure models described above were used in the ferrite phases of the DP600, DP800, and DP1000 steels. Meanwhile, in the ferrite phase, the ferrite flow curves of Figure 4 were set in Mat_Gurson and Mat_Gurson_JC, whereas in Mat_Johnson_Cook, the respective parameters defining the flow curve were used.

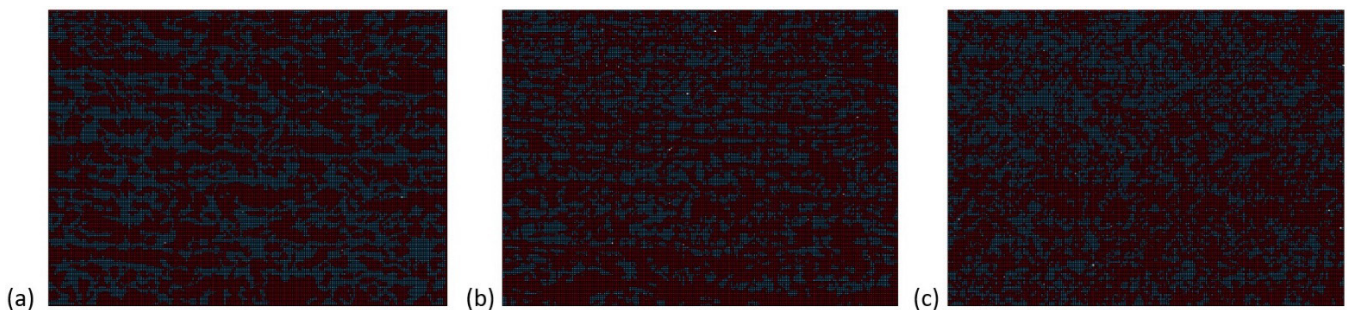


Figure 6. Finite element specimens of DP steels (red phase ferrite, blue phase martensite), a) DP600, b) DP800, and c) DP1000

4 RESULTS AND DISCUSSION

4.1 Parameters determination and comparisons of experimental and numerical flow curves FE

Uniaxial tensile test simulations of 2D microstructure specimens were performed on the LS-DYNA software with three different damage models using Gurson_120_Mat, Gurson_JC_120_Mat, and Johnson_COOK_0.15_Mat models. Significantly, the parameters of the aforementioned model were obtained through the baseline optimization process of the microstructure specimens of DP600, DP800, and DP1000 steels. Using the introduced parameters and flow curve models, finite element simulations of the 2D RVE model under uniaxial tensile loads were carried out. All the parameters belonging to each model used in these studies were determined for ferrite phase by the basic optimization process through LS-OPT (Tables 4 to 8). The GTN parameters are listed in Table 4 the Gurson-Johnson-Cook parameters are listed in Tables 5, 6, and 7 and the Johnson-Cook parameters are listed in Table 8.

Table 4. GTN parameters of 2D DP600, DP800, and DP1000 steels

| Specimens | Parameter | ϵ_N | f_c | f_f | f_N | q_1 | q_2 | S_N |
|---------------------------------|-----------|--------------|---------|--------|---------|-------|-------|-------|
| DP600, 2D 125*93 μm | | 0.09 | 0.01083 | 0.1315 | 0.00218 | 1.25 | 0.7 | 0.03 |
| DP800, 2D 125*93 μm | | 0.03 | 0.01283 | 0.2115 | 0.00418 | 1.15 | 0.8 | 0.03 |
| DP1000, 2D 125*93 μm | | 0.03 | 0.00883 | 0.2116 | 0.00718 | 1.15 | 0.81 | 0.031 |

Table 5. GURSON_JC_120_MAT; parameters of DP600 steel; 2D 125*93 μm

| ϵ_N | f_c | f_f | f_N | q_1 | q_2 | S_N | D1 | D2 | D3 | D4 | L1 | L2 |
|--------------|----------|----------|----------|-------|-------|-------|------|------|-----|-----|----|-------|
| 0.09 | 0.010836 | 0.131573 | 0.002186 | 1.25 | 0.7 | 0.2 | 2.65 | 0.05 | -01 | 0.1 | 1 | 0.015 |

Table 6. GURSON_JC_120_MAT; parameters of DP800 steel; 2D 125*93 μm

| ϵ_N | f_c | f_f | f_N | q_1 | q_2 | S_N | D1 | D2 | D3 | D4 | L1 | L2 |
|--------------|----------|----------|---------|-------|-------|----------|-------|-----|----|----------|----|-------|
| 0.31 | 0.020836 | 0.111157 | 0.00118 | 1 | 0.8 | 0.006662 | 2.625 | 0.3 | -2 | 0.123143 | 1 | 0.015 |

Table 7. GURSON_JC_120_MAT; parameters of DP1000 steel; 2D 125*93 μm

| ϵ_N | f_c | f_f | f_N | q_1 | q_2 | S_N | D1 | D2 | D3 | D4 | L1 | L2 |
|--------------|---------|----------|----------|-------|-------|----------|-------|-----|----|---------|----|-------|
| 0.31 | 0.01084 | 0.111115 | 0.001186 | 1 | 0.81 | 0.006662 | 1.105 | 0.3 | -2 | 0.12314 | 1 | 0.015 |

Table 8. Johnson–Cook parameters of 2D DP600, DP800, and DP1000 steels

| Specimens | Parameter | A | B | n | C | D1 | D2 | D3 | D4 |
|---------------------------------|-----------|-----|-----|------|---------|--------|-------|----|----------|
| DP600, 2D 125*93 μm | | 279 | 370 | 0.38 | 0.08495 | 0.7525 | 0.35 | -9 | 0.133143 |
| DP800, 2D 125*93 μm | | 275 | 400 | 0.38 | 0.08495 | 0.7025 | 0.345 | -9 | 0.133151 |
| DP1000, 2D 125*93 μm | | 276 | 385 | 0.38 | 0.08349 | 0.5205 | 0.36 | -9 | 0.133203 |

Using the introduced parameters, finite element simulations of the 2D RVE model under uniaxial tensile loads were carried out. And the standard experimental (EXP) and simulation (SIM) true stress–strain curves were compared in terms of the microstructure samples. For each DP steel, the relative errors (RE) between comparisons calculated at fracture strain are provided as a percentage. Additionally, the simulation true stress strain curves of (Çavuşoğlu et al. 2019) are used as comparative curves.

Figure 7 compares the true stress strain curves of EXP and SIM as a result of Gurson model parameters. Therefore, Figure 7 (a) shows the comparisons corresponding to the DP600 steel, wherein there is an acceptable fit between the EXP and SIM curves, while the measurement RE at fracture strain is about 0.8%. Similar to those in Figure 7 (b), wherein the comparisons corresponding to the DP800 steel are presented with an acceptable fit, herein, the RE is about 5.5%. Figure 7 (c) compares the EXP and SIM results, where RE at fracture strain is about 3.3%. In this case, the simulation curve is slightly lower than the reference curves in terms of the true stress. And the measurement RE at fracture strain is about 3.3%.

Figure 8 compares the true stress strain curves of EXP and SIM as a result of Gurson–Johnson–Cook model parameters. Thus, Figure 8 (a) shows the comparisons corresponding to DP600, wherein an acceptable fit between the EXP and SIM curves is observed, while the measurement RE at fracture strain is about 1.7%. Similarly, Figure 8 (b) shows the comparisons corresponding to DP800, wherein an acceptable fit between the curves is observed. In this case, the RE is about 4.1%. Figure 8 (c) compares the EXP and SIM results, where RE at fracture strain is about 4.3%. In this case, the simulation curve is slightly lower than the reference curves in terms of the actual stress. However, it is more definite than the curve obtained from the Gurson model for the same sample.

Finally, Figure 9 compares the true stress strain curves of EXP and SIM as a result of Johnson–Cook model parameters. Moreover, Figure 9 (a) shows the comparisons corresponding to DP600, where an acceptable fit is observed between the EXP and SIM curves, while the RE is about 0.7%. Similarly, Figure 9 (b) shows the comparisons corresponding to DP800 with an acceptable fit. Herein, the RE is about 1.4%. Whereas in Figure 9 (c), the comparisons between the EXP and SIM results for DP1000 steel, the measurement RE at fracture strain is about 5.8%. In this case, the SIM curve is slightly lower than the REF curves in terms of the true stress. However, it is higher than the curves obtained from the Gurson and Gurson JC models for the same sample.

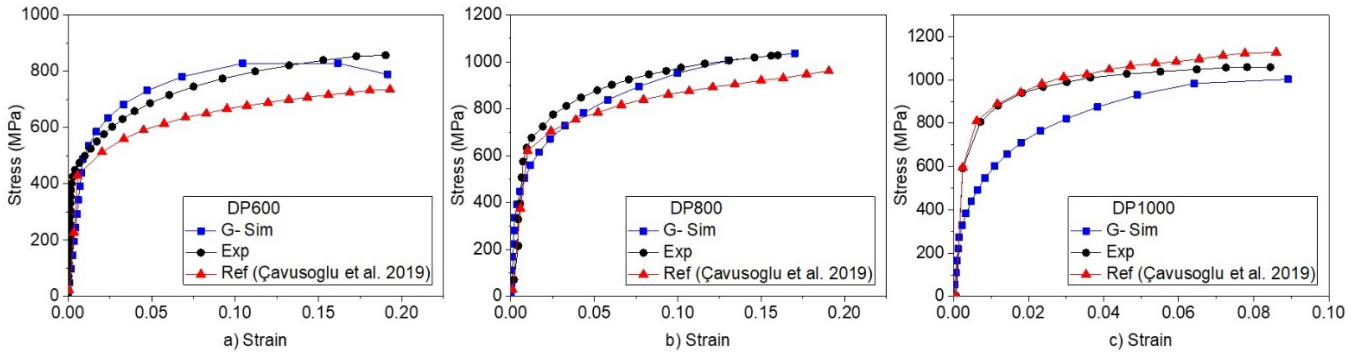


Figure 7. Comparisons between experimental and 2D true stress–strain responses of the investigated DP steels derived from the Gurson model.

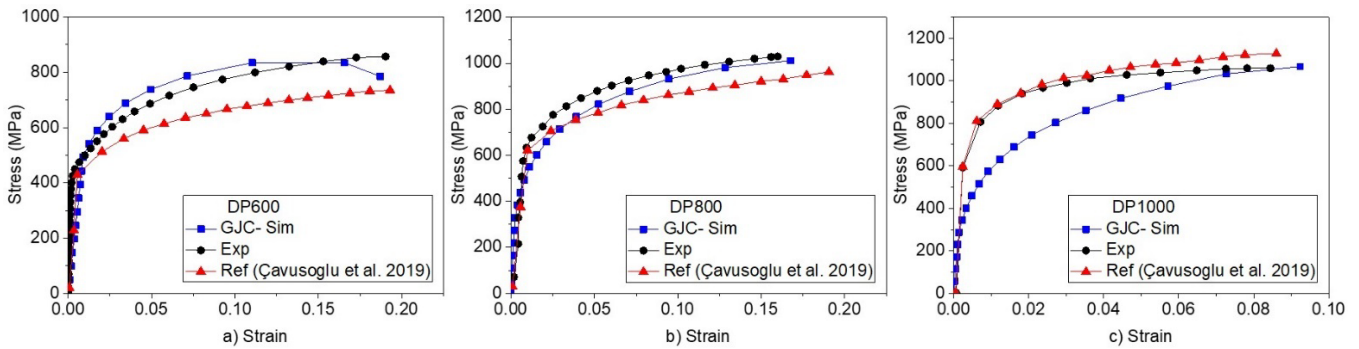


Figure 8. Comparisons of the Gurson-Johnson-Cook model's true stress-strain values from the DP600, DP800, and DP1000 experimental and numerical approaches

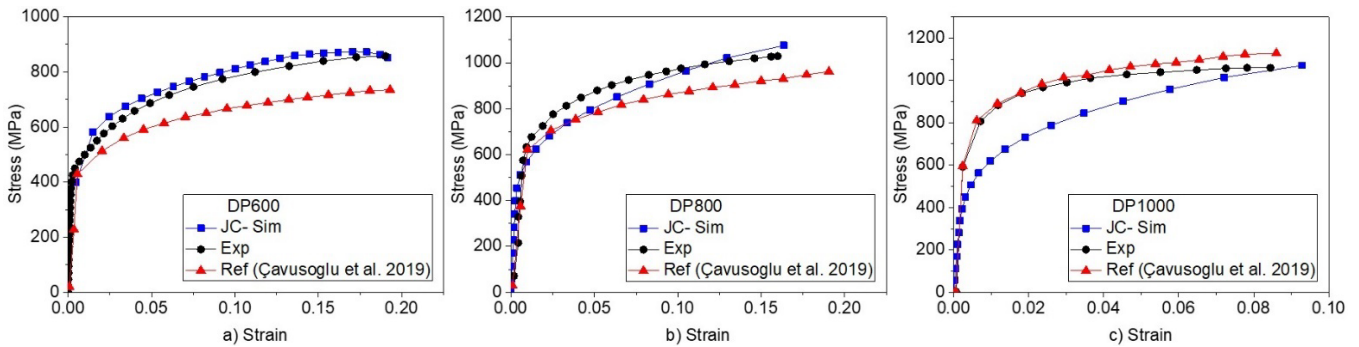


Figure 9. Comparisons of the investigated DP steels' true stress-strain responses, as measured experimentally and numerically using the Johnson Cook model.

4.2 Comparisons of stress distribution of DP steels with different failure models

In this study, the stress distributions of the ferrite and martensite phases of these steels were presented. Measurements were performed in three stages of deformation, expressed in percentages of the micron strain values. In addition, for the DP600 and DP800 steels, the measurement in percentage was ~1-2% yield stress, ~8% plastic strain, and ~15-17% ultimate tensile strength, i.e., where the onset of crack occurs; for the DP1000 steel, the corresponding measurements were 1%, 5%, and 9%, respectively, as the elongation scale of DP1000 is evidently smaller than that of the other two steels. Table 8 lists the stress distribution resulting from each model used, and the true stress distribution is presented for the ferrite and martensite phases of the investigated steels. Table 9 shows the comparisons between the numerical, experimental, and referenced results of Çavuşoğlu *et al.* (2019). Furthermore, Figures 9, 10, and 11, represent the corresponding von Mises stress distributions by comparing them at three strain stages with three different damage/failure models. Plastic incompatibility increases the average applied stress at the hard phase above the mean stress value in dual-phase alloys according to (Szewczyk and Gurland. A.F. 1982). They discovered that the local uniaxial stress of martensite could be three times that of ferrite. Consequently, the martensite phase was subjected to a relatively substantial local stress when a large plastic strain was applied. This phenomenon was also observed in this study.

Table 9. Stress distribution corresponding to phases of DP steels at three different stages (%) by three different damage models

| Model | Strain | Gurson | Gurson JC | Johnson Cook | EXP | Reff Çavuşoğlu <i>at al.</i> (2019) | Gurson | Gurson JC | Johnson Cook | Reff Çavuşoğlu <i>at al.</i> (2019) |
|--------|--------|-------------|-------------|--------------|-------------|-------------------------------------|----------|-----------|--------------|-------------------------------------|
| Steels | ε % | Ferrite MPa | Ferrite MPa | Ferrite MPa | Ferrite MPa | Ferrite MPa | Mart MPa | Mart MPa | Mart MPa | Mart MPa |
| DP600 | 1.00 | 410.72 | 414.53 | 441.34 | 405.11 | 399.89 | 845.54 | 847.23 | 817.71 | 799.9 |
| | 8.00 | 601.07 | 640.40 | 596.15 | 559.20 | 566.49 | 1513.67 | 1508.42 | 1508.42 | 1465.7 |
| | 17.00 | 694.76 | 709.23 | 719.9 | 675 | 637.93 | 1661.35 | 1656.15 | 1743.32 | 1591.5 |
| DP800 | 1.00 | 399.13 | 406.2 | 442.3 | 420 | 445.18 | 762.15 | 763.12 | 815.91 | 834.64 |
| | 8.00 | 624.79 | 631 | 606.47 | 566 | 528 | 1406.18 | 1394.75 | 1439.87 | 1436.7 |
| | 15.00 | 694.17 | 732.3 | 716.9 | 648 | 613.13 | 1653.32 | 1595.89 | 1745.62 | 1594 |
| DP1000 | 1.00 | 481.97 | 480.51 | 442.85 | 445 | 484 | 775.11 | 779.47 | 818.49 | 819.3 |
| | 5.00 | 658.09 | 662.06 | 548.58 | 644.63 | 646.27 | 1322.56 | 1529.99 | 1327.91 | 1554.9 |
| | 9.00 | 670.08 | 686.83 | 613.41 | 672.40 | 672.13 | 1446.5 | 154038 | 1565.67 | 1709.4 |

4.3 Stress distribution of DP600 steel according to different damage models

The von Mises stress distribution of the three different models of DP600 steel is shown in Figure 10. Herein, the stage of deformation is ~1%, and there is no significant difference in the stress distributions between the models. However, the largest stress appears across the martensite grains, and the distribution is proportional to the hole surface. Furthermore, when the measurement of stress distribution was performed at 8%, there were no significant differences between the models, but stress concentration was distributed in all the martensite grains and developed, especially in those grains that were larger and longer. The measurement of stress in the phases was performed as per (Sawitree et al. 2012), who emphasized that the micromechanical model could be used to describe the local stress and strain development of the individual phases in the DP microstructures. Moreover, by measuring the stress at 17% elongations in this case, the stress was slightly more pronounced in the martensite phase in the JC model than the other two models; in contrast, in the ferrite phase, it was 10 MPa higher than that of the other two models.

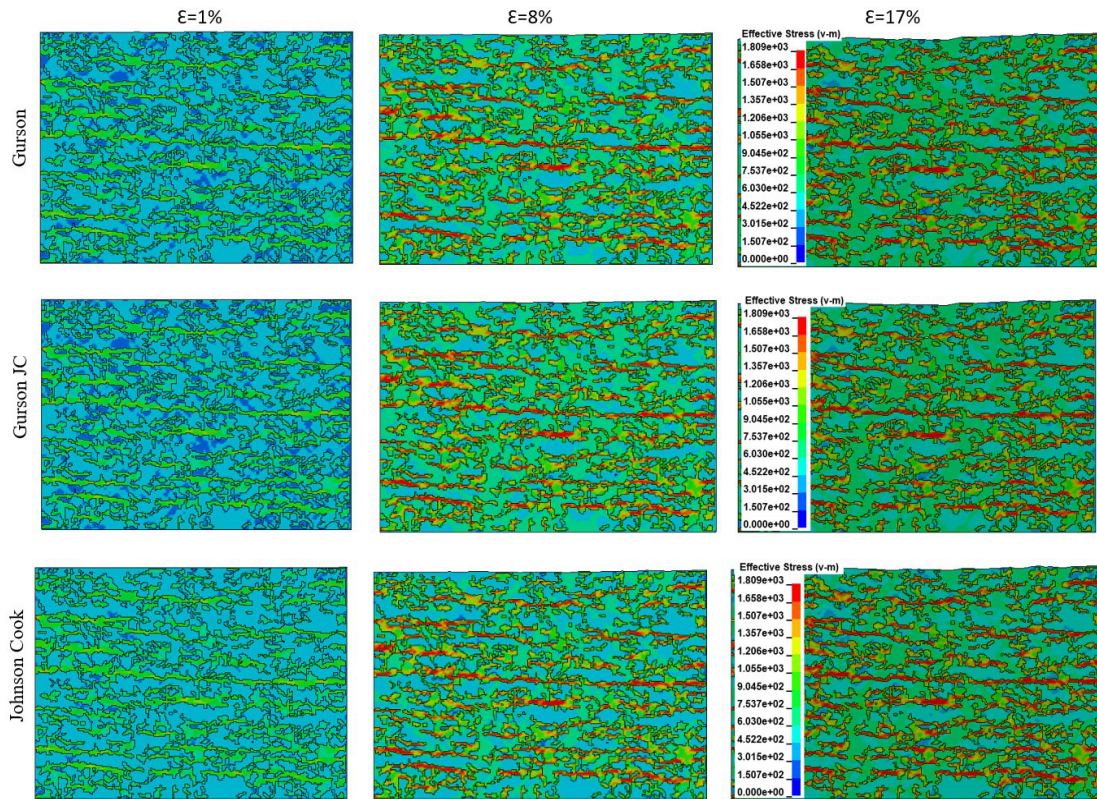


Figure 10. von Mises stress distribution of DP600 steel at three deformation stages

4.4 Stress distribution of DP800 steel according to different damage models

Figure 11 shows the von Mises stress distribution of the three distinct models of DP800 steel. In this example, the yield strength is observed to be 1%, and the Johnson–Cook model has the largest stress distribution among the two phases. The highest stress is also observed in the martensite grains, with a proportionate distribution on the hole surface. Furthermore, when the stress distribution was measured at 8%, no differences were found between the Gurson and Gurson–JC models. However, the most significant variation was observed in the Johnson–Cook model, wherein when compared to the other two models, the stress appeared to be higher in the martensite phase and lower in the ferrite phase. However, as the stress was distributed in the martensite grains and developed, especially in those that were larger and longer, a larger stress did not appear in the smaller grains, whereas in the ferrite grains, there did not seem to be a stress concentration, similar to the findings of (Zhou et al. 2015). Furthermore, by measuring the stress distribution at 15% elongation, the stress was slightly more pronounced in the martensite phase in the Johnson–Cook model than in the two other models; in this case, the stress was slightly more pronounced in the ferrite phase in the Gurson–JC model than in the other two models.

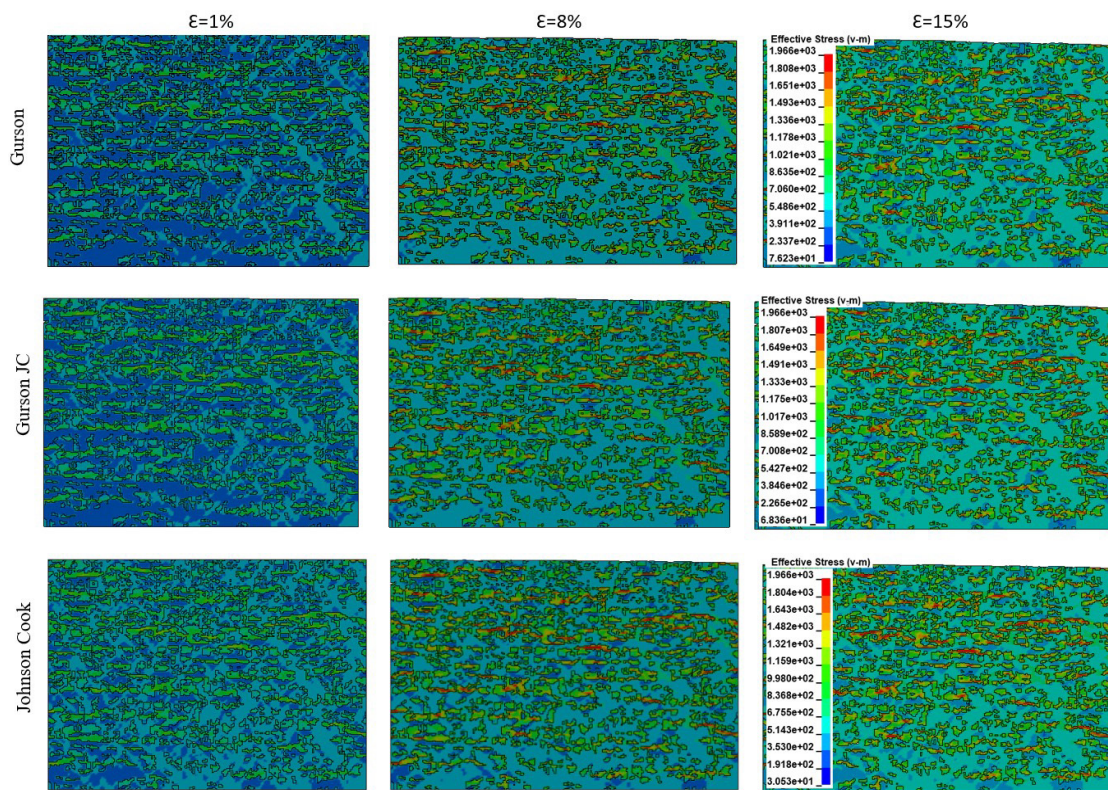


Figure 11. von Mises stress distribution of DP800 steel at three deformation stages

4.5 Stress distribution of DP1000 steel according to different damage models

Figure 12 depicts the von Mises stress distribution of the three DP1000 steel models. The yield strength is evident at stage 1% in this example, and the Johnson–Cook model has the largest stress distribution in the two phases. The maximum stress distribution is also found in the largest and longest martensite grains and is unique. Furthermore, no differences were detected between the Gurson and Johnson–Cook models when the stress distribution was examined at the 5% level. The largest substantial change is observed in the Gurson–JC model, where the stress is larger in both stages than those in the other two models. However, compared to the other two steels, stress is distributed more evenly in the large martensite grains, whereas it does not appear to be concentrated in the ferrite grains. Furthermore, the stress is significantly more evident in the martensite phase in the Johnson–Cook model than in the other two models, whereas it is slightly more pronounced in the ferrite phase in the Gurson–JC model than in the other two models when measured at 9% elongation.

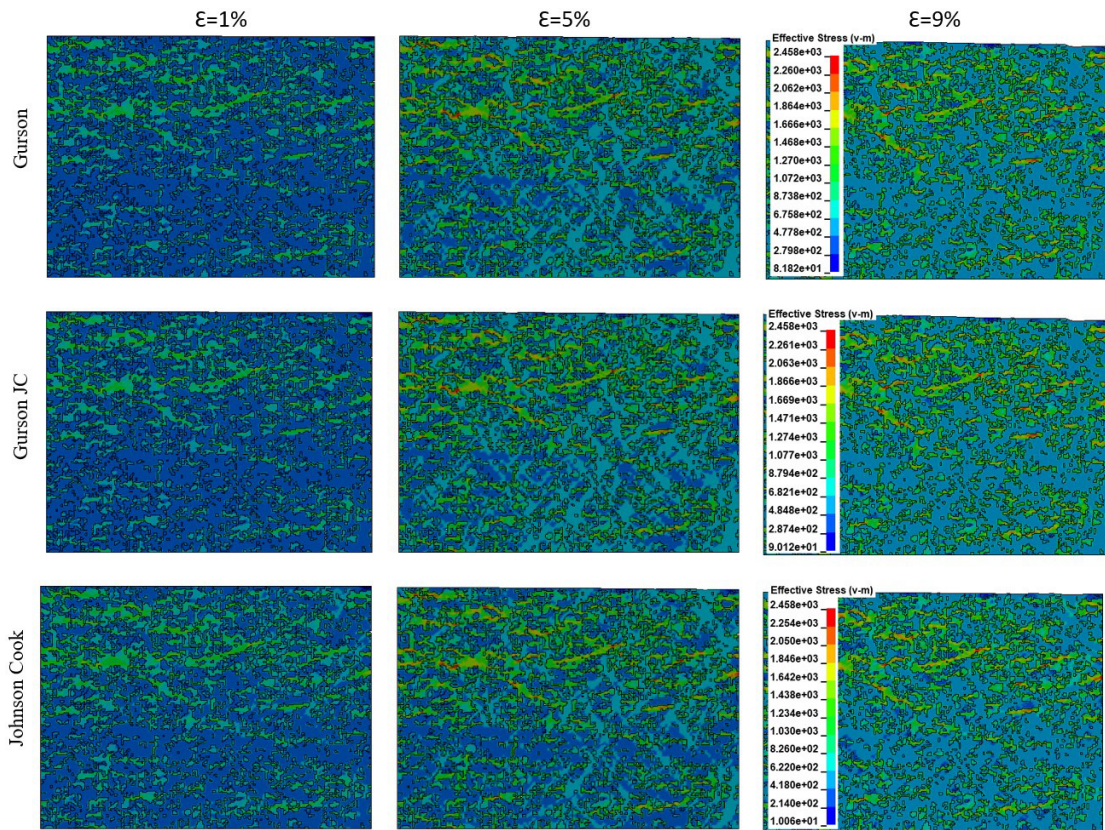


Figure 12. von Mises stress distribution of DP1000 steel at three deformation stages

4.6 Strain distribution of DP600 steel according to different damage models

This study was based on the results of the simulations performed with the three damage models mentioned above. The distribution of the effective plastic strain across the ferrite and martensite phases is shown in Figure 13, for DP600 steel, respectively. The effective plastic strain distribution at three deformation stages was expressed in percentages of micron-scale strain values. The effective plastic strains at 1%, 8%, and 15% are presented for the DP600 steel.

The figures created within the scope of the study show that the strain distributions occur with deformation in the phases within the microstructure. It is also shown how these distributions vary with different models. When the distributions of this strains in the microstructure of the materials are examined in detail, it is understood that differences are seen depending on the topological properties and loading direction of the martensite phases in the internal structure and the orientations they have made. Within the scope of the study, unit shape changes in the internal structure were intended to be given for this purpose.

Figure 13 shows the simulation result of the microstructure plastic strain with the Gurson (G), Gurson-Johnson-Cook (GJC), and Johnson-Cook (JC) models to the 17% elongation corresponding to the deformation stage expressed as Effective Plastic Strain (EPS): EPS of the G model is $1.945e+00$, EPS of the GJC model is $1.896e+00$, and EPS of the JC model is $1.173e+00$ (see colored legend in Figure 13). It is worth noting that at these stages of deformation, localized necking is initiated but crack propagation has not yet begun, and crack propagation begins after these values.

The plastic strain in the figure is visible at all measurement scales and covers the entire surface of the ferrite phase; this proportional elongation phenomenon occurred because the martensite grains in DP600 are more elongated in most cases or are found related to one another.

Additionally, it appears that the ferrite phase had a proportional elongation in the three models where the elongation was 1%. While in the JC model, the elongation in the ferrite phase continues to be more proportionate. The most noticeable plastic strain arises in the middle of the sample when measurements were conducted at an elongation of 8% in the Gurson and Gurson JC models. Even when measurements were taken at 15% elongation, the Gurson and Gurson JC models still show a similar plastic strain, but the location of the later-occurring cracking

or breaking of the sample shows higher elongation concentrated in the ferrite phase. On the other hand, the elongation is still spread across the sample's surface in the Johnson-Cook model.

In the comparisons made between the models regarding the effective plastic strain, it is clear that the Gurson and Gurson JC models have similarities in all stages of the measurements. On the other hand, the Johnson-Cook model has the most pronounced difference when the measurement is made in the 15% extension. This difference occurs because the shape of the flow curve of this model is generally more linear than the flow curves of the comparative models (see Figures 7 (a), 8 (a), and 9 (a)).

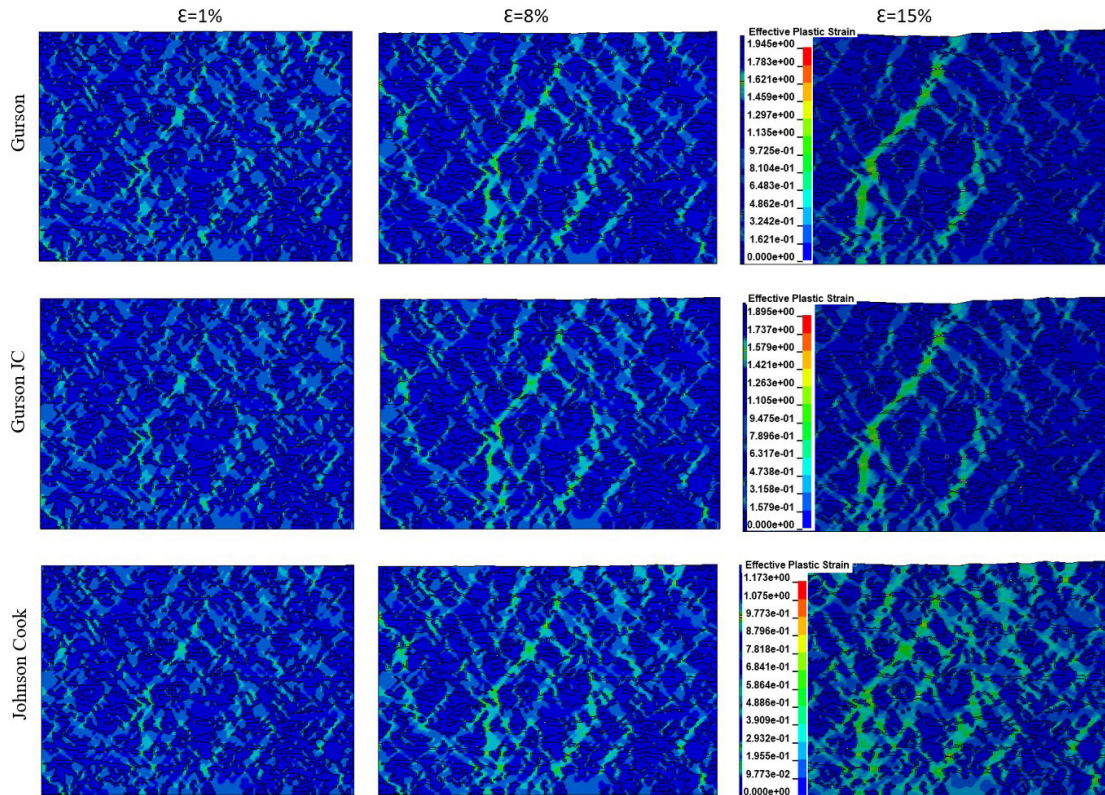


Figure 13. Effective plastic strain distribution of DP600 steel at three deformation stages

4.7 Strain distribution of DP800 steel according to different damage models

In Figure 14 the differences between the models were examined with a focus on the effective plastic strain. In this case, although the percentage of the martensite phase in DP800 steel is higher than in DP600 steel, from the figure, it can be seen that the martensite grains do not appear to be very connected to each other. For this reason, plastic strain is more concentrated in some ferrite areas, which usually have a smaller distribution of the martensite phase and where the smallest grains of the martensite phase are mainly found. Figure 14 shows the simulation result of the microstructure plastic strain with the abovementioned models to the 15% deformation stage. Herein, EPS of the G model is 1.530e+00, EPS of the GJC model is 1.572e+00, and EPS of the JC model is 1.129e+00 (see colored legend in Figure 14). In addition, at these stages of deformation, localized necking is initiated but crack propagation has not yet begun, and crack propagation begins after these values.

The study's objects were DP800 steel, respectively. Similar to the prior instance, there isn't a significant difference between the models' extension distributions for extensions of 1%. In the Gurson and Gurson JC models, the elongation has started to concentrate in the same area, whereas in the Johnson-Cook model, the elongation has continued to be dispersed over the entire surface when the plastic strain was measured at an elongation of 8% for DP800 steel. However, when measurements were taken in the Gurson and Gurson JC models at an elongation rate of 15% close to the time of crack onset, the elongations appeared to be localized there. In contrast, the plastic strain in the Johnson-Cook model appears to be distributed across several areas of the sample's surface rather than appearing to be concentrated in one location.

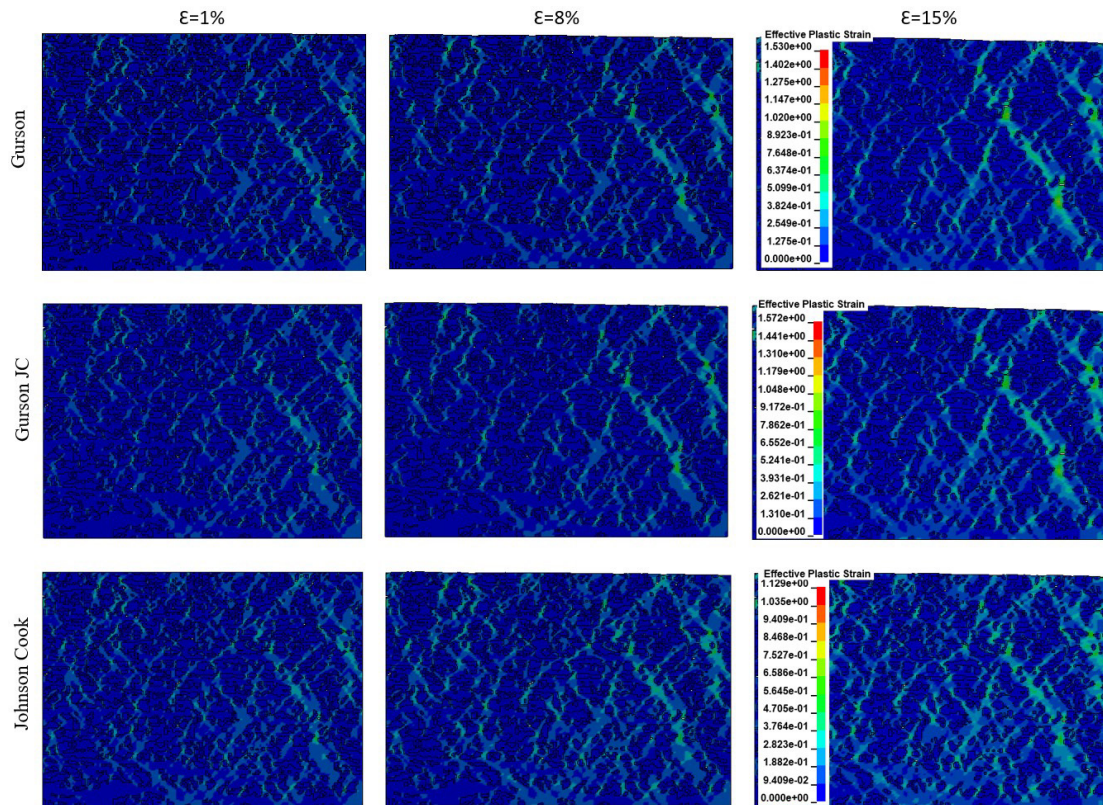


Figure 14. Effective plastic strain distribution of DP800 steel at three deformation stages

4.8 Strain distribution of DP1000 steel according to different damage models

Figure 15 shows that there were no obvious differences between the models in terms of the concentration of the extensions in a particular area when the study's subject was DP1000 steel and where measurements were taken at 1% and 5% extensions. The Gurson and Gurson JC models are very similar in the locations of strain concentrations, while the Johnson-Cook model extensions are more widespread in many places on the surface of the sample, with emphasis in those areas where the martensitic grains are tiny. Furthermore, as shown in the figures below, the concentration of plastic strain in DP1000 steel is concentrated in some pronounced areas from the start of elongation. Figure 15 shows the simulation result of the microstructure plastic strain with the mentioned models to the 9% deformation stage wherein, the G model's EPS is 1.276e+00, the GJC model's EPS is 1.241e+00, and the JC model's EPS is 8.609e-00 (see colored legend in Figure 15). Likewise, at these stages of deformation, localized necking is initiated but crack propagation has not yet begun; it begins after these values.

The differences between the models were observed up to the extensions having reached the moment of crack initiation. In addition, there were no noticeable differences between the Gurson and Gurson_JC reagents' effective plastic strain distributions; even from the figures, the strain concentration is almost similar in all the stages of deformation. However, there are differences between the other two models and Johnson-Cook damage model; from the comparisons of the figures, the strain concentration is distributed almost uniformly or homogeneously over all the ferrite surfaces of the samples at all the stages of deformation. The effective plastic strain was similar to that in the study by Çavuşoğlu *et al.* (2019).

4.9 Investigation of fractures in numerical simulations of DP steels according to different damage models

An example of crack propagation through simulations is presented in Figure 16. Typically, a fracture initiates within the martensite islands. However, the findings of the current investigation demonstrated that nucleation occurred in both the martensite and ferrite phases, with the voids formed within the ferrite phase near the martensite boundary being more prevalent. These voids then elongated because of the applied deformation, forming microcracks. These cracks, in turn, propagated within the martensite islands or ferrite grains. When no other route existed for fracture propagation, the crack propagated through the martensite grains. Another representative comparison of the crack locations and practices between the failure models and experimental crack propagation is shown in Figure 17. Furthermore, the crack propagation resulting from the simulations performed on LS-DYNA with the Gurson, Gurson-Johnson-Cook, and

Johnson–Cook models for steels are shown in Figures 18, 19, and 20 for DP600, DP800, and DP1000 steels, respectively. In this study, the main focus was on the onset of steel cracking (crack initiation), void nucleation, void growth, and coalescence. Lastly, the crack mechanism in reel microstructure and comparisons of the cracks in the used damage models for each steel is shown separately in the following figures through the deleted elements.

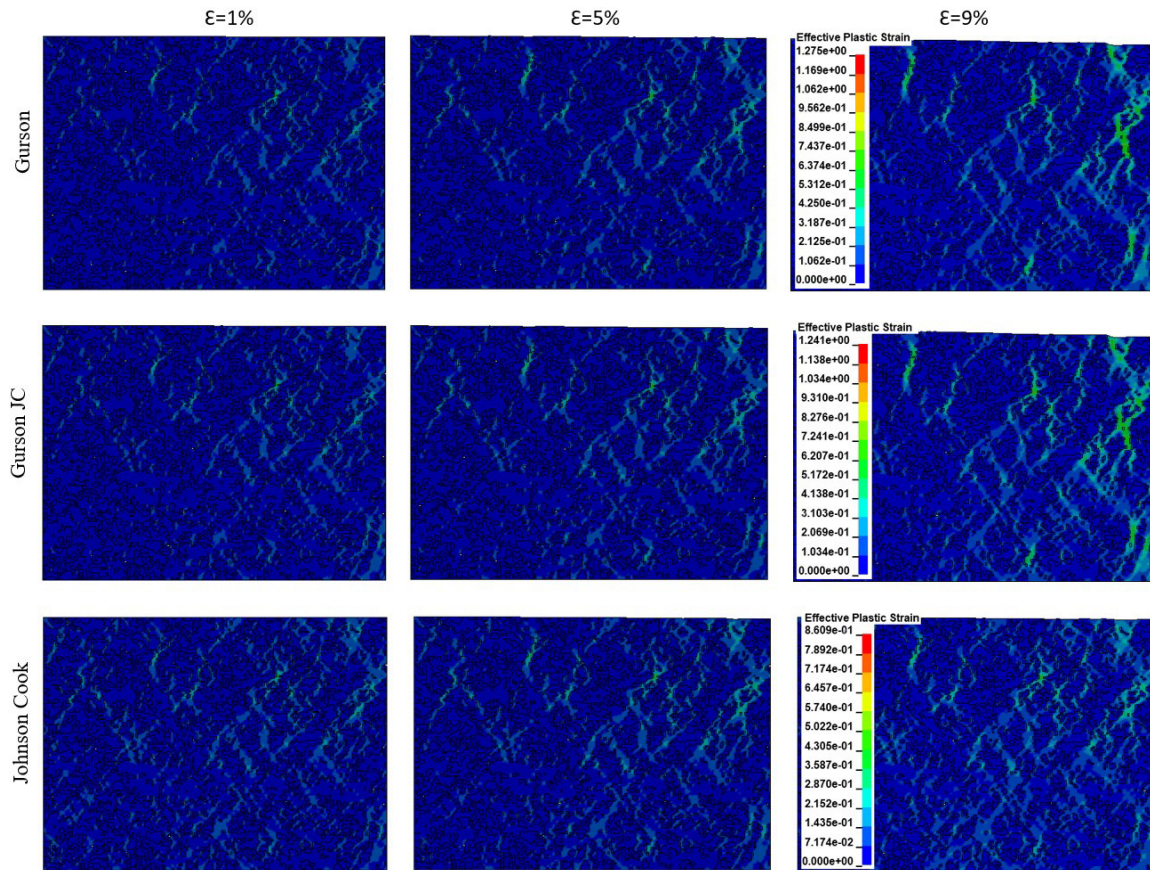


Figure 15. Effective plastic strain distribution of DP1000 steel at three deformation stages

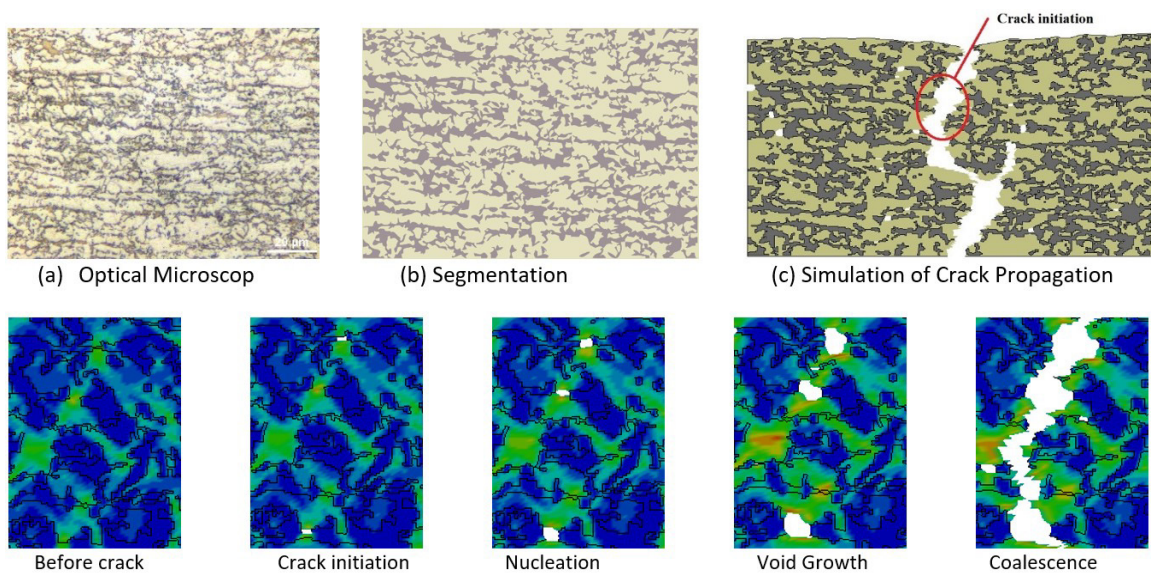


Figure 16. Crack propagation through simulations

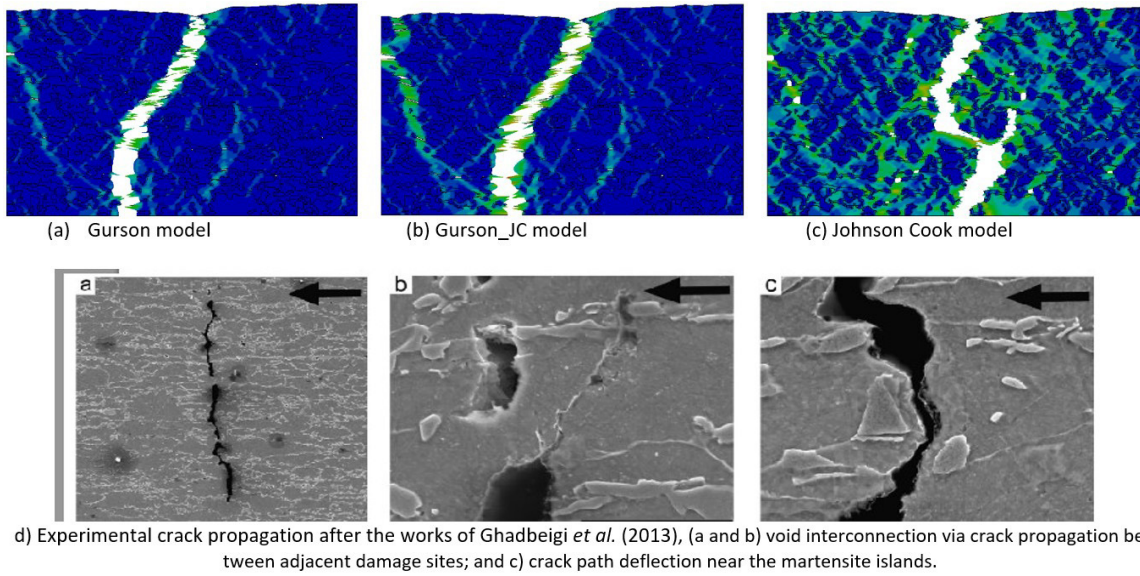


Figure 17. Comparison of cracks between numerical failure models and experimental crack propagation

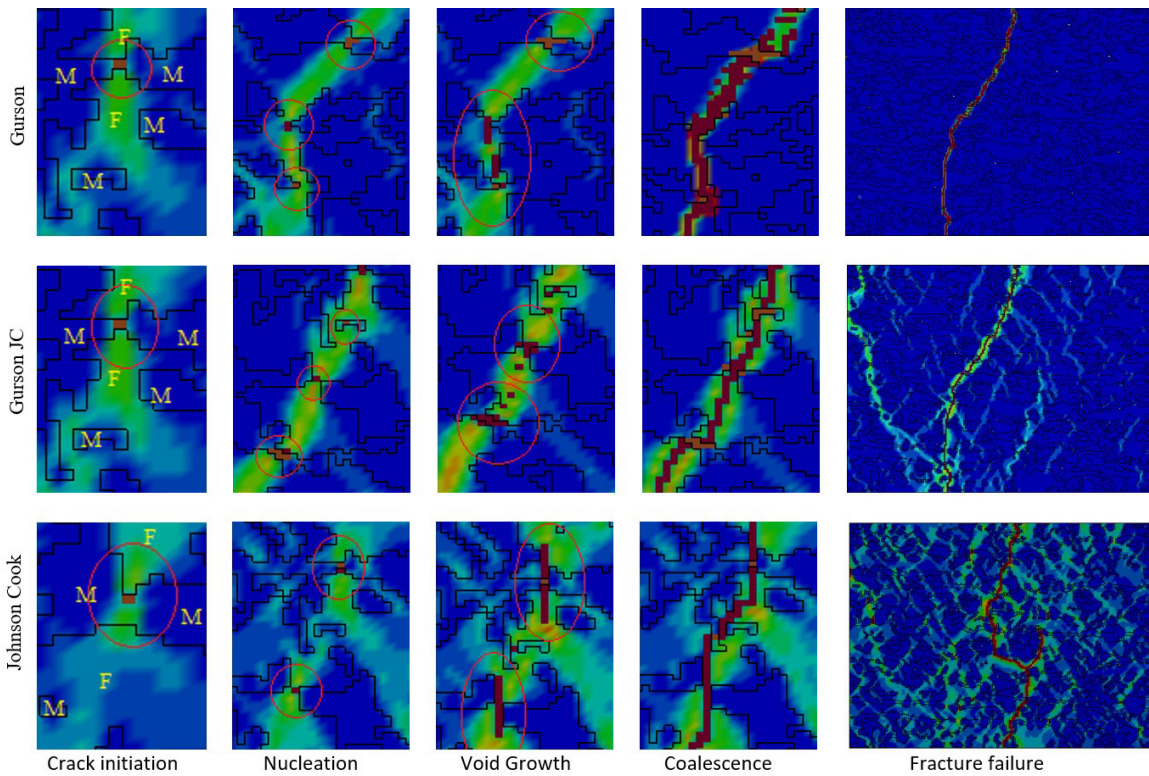


Figure 18. Crack propagation of DP600 steel according to different models

4.9.1 The fracture characteristics of DP600 steel

Figure 18 shows the crack propagations of DP600 steel resulting from the simulations of the three different damage models. Here, it can be understood that it is possible to reach different stress values and crack locations, especially in regions where different triaxiality values are formed, and that the topological properties of the phases significantly affect the ability of the materials to be shaped. Within the scope of the study, the crack locations by different damage models in the internal structure were intended to be given for this purpose. In this case, the crack initiations occur mainly in the martensite grains, which means that the triaxiality is greater than on all internal surfaces of specimens. This phenomenon of martensite failure evident as the onset of crack illustrated in the finite element modeling is similar to that observed in the experimental research conducted for DP600 steels by (Ghadbeigi et al. (2013)). While void nucleation is a known phenomenon in fracture micromechanics, (Lassance et al. (2006) stated that small particles were more likely

to be spherical or equiaxed, stimulating interface fracture. As per the simulation of DP600 steel, void nucleation also occurred in the martensite phase. This was proved by three models, as shown in Figure 18. However, the void growth and coalescence occur and continue to propagate through the ferrite phase, which is also proved by the three-damage model. Upon comparing the crack propagation between the models, the Gurson and Gurson–JC models do not exhibit a noticeable difference in their crack location, whereas the Johnson–Cook model exhibits a different location of crack propagation compared with the other two models (see Figure 18).

4.9.2 The fracture characteristics of DP800 steel

Figure 19 depicts crack propagation in the DP800 steel as a result of three distinctly simulated damage models. In this example, metal ductility decreases with increasing stress triaxiality, which is a significant influencing factor. Furthermore, the crack initiation occurred in the martensite grains supplied by the Gurson and Gurson–JC models. Moreover, the crack initiation occurs mostly through the martensite islands according to the SEM microstructure observation of DP steel by (Sirinakorn et al. (2014), which is similar to our findings. Compared with the two other models, the crack initiation in the Johnson–Cook model occurred at the ferrite phase. Also, when the study object was the internal structure of DP800 steel, the largest stress triaxiality occurs at the crack initiation. Furthermore, the void nucleation occurred between the two martensite grains and through the ferrite phase, as proved by the three models, as shown in Figure 19. In contrast, the void growth and coalescence occurred and continued to propagate between the martensite grains and through the ferrite phase. This was also proved by the three damage models. (Toda et al. 2017) proposed that because of martensitic cracking, an additional damage develops, primarily near the tight ferrite/martensite interfaces and intersections between the martensite and ferrite grain boundaries. Upon comparing the crack propagation among the models, the Gurson and Gurson–JC models do not exhibit too many noticeable differences in their crack locations, whereas the Johnson–Cook model exhibits a different location of crack propagation, as shown in Figure 19.

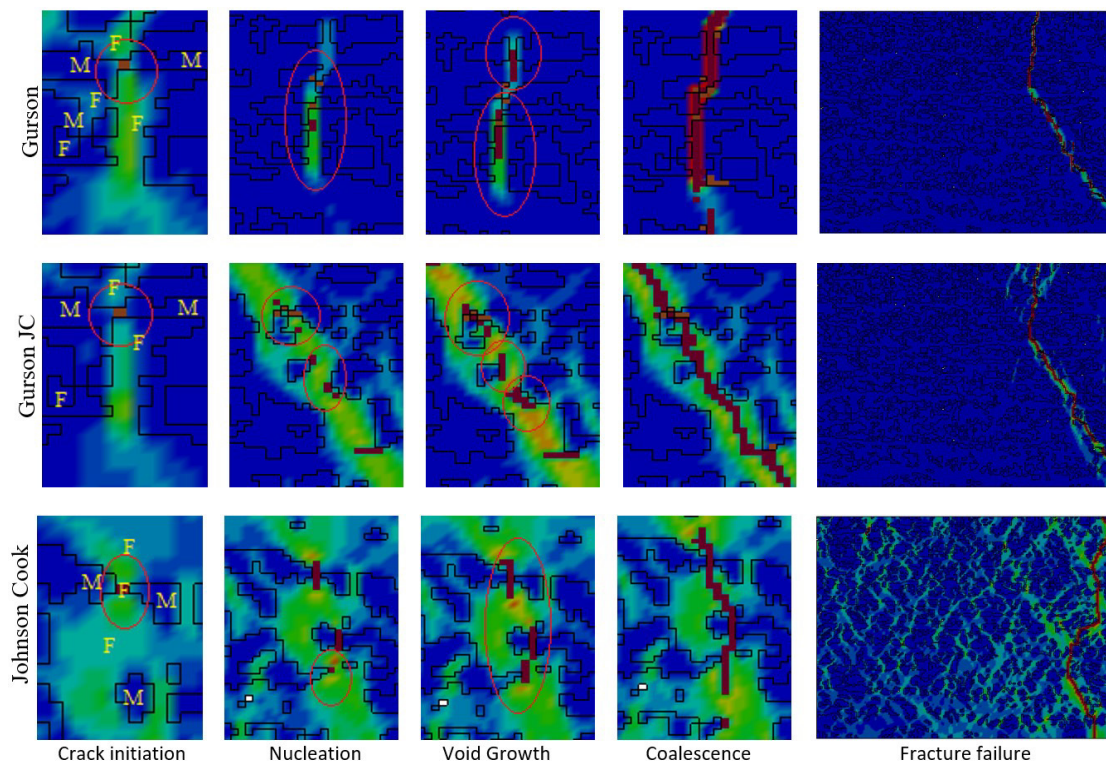


Figure 19. Crack propagation of DP800 steel according to different models

4.9.3 The fracture characteristics of DP1000 steel

From Figure 20, considering the crack propagation in the DP1000 steel, in contrast with the DP600 and DP800 steels, no cracking is present in the martensite phase, as it has the highest percentage of C, i.e., up to 0.45%, which highly strengthens it, and the entire cracking process occurs in the ferrite stage. Therefore, the crack distribution occurred similar to the simulations based on (Çavuşoğlu et al. 2019), which stated that the ferrite phase trapped between the martensite grains initiated the crack propagation.

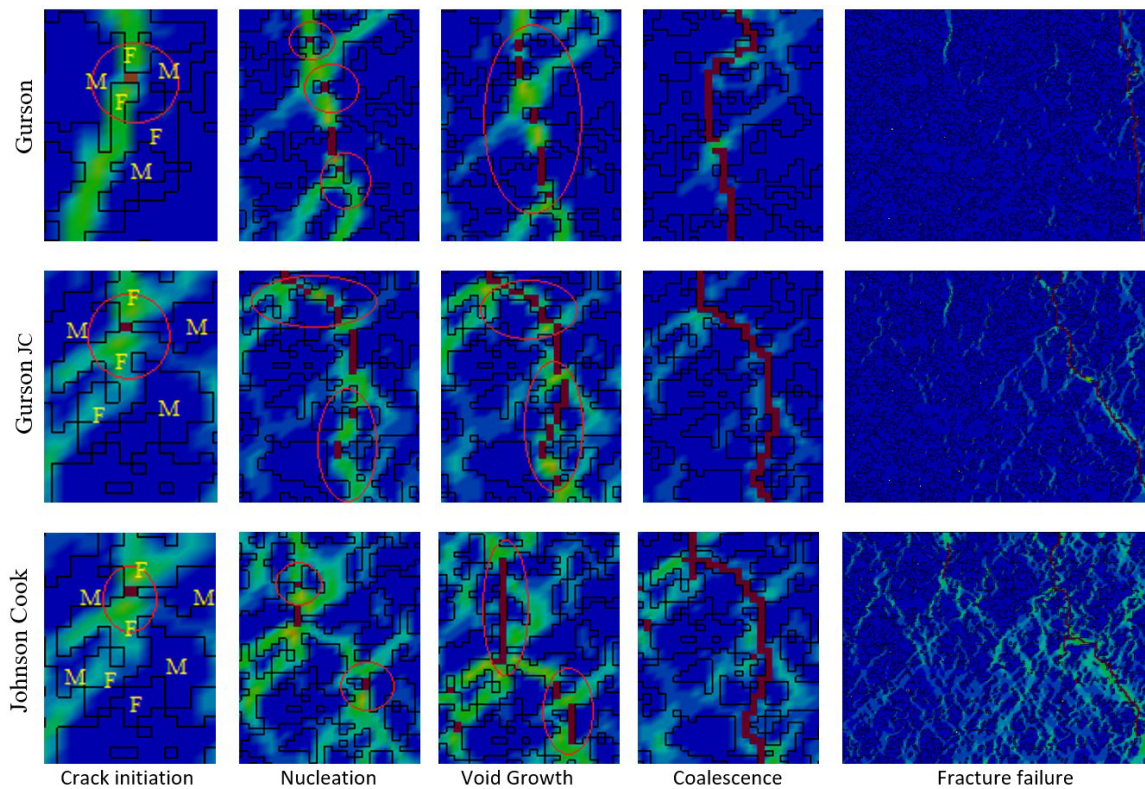


Figure 20. Crack propagation of DP1000 steel according to different models

CONCLUSIONS

The focus of this research on real 2D microstructures using the finite element approach was to determine the parameters of the Gurson 120 MAT, Gurson-Johnson-Cook 120 MAT, and Johnson-Cook 098 MAT models. The determination of these parameters of the abovementioned models was made for the ferrite (ductile) phase of DP600, DP800, and DP1000 steels. After calibration and optimization of these parameters, outcomes, such as stress distribution, effective plastic strain, and crack propagation, of different models were defined, and the results were compared between the different models. Moreover, to validate the results, the true stress-strain curves obtained from different 2D simulated models were compared with the corresponding experimental results in terms of stress-strain curves. The comparative scale of accuracy between the models is made at the fracture strain, based on the comparison of the experimental results with the results of the numerical simulations. In conclusion, the average accuracy in the Gurson model is 3.33%, the Gurson JC model is 1.82%, and the Johnson Cook Model is 2.39%.

Additionally, the true stress of three different microscopic DP steel plates was measured at three different stages of deformation from 1–17%. And the experimental results of the true stress of the ferrite phase were compared with the results of the three models used. When the deformation stages were 1–17%, no significant difference in the stress distributions appeared between the comparisons. It is necessary to mention the stress concentrations in the grains, where the highest stress occurs in the largest martensite grains. Because of this, the stress distribution was not proportional to the entire surface. Moreover, measuring the stress at the final stage of the deformations, it was slightly more pronounced in the martensite grains, mainly near the fracture site.

In addition, regarding effective plastic strain distributions, there were no noticeable differences between the Gurson and Gurson_JC models. The strain concentration is almost similar at 1%, 8%, 9%, and 15% of the deformations of DP600, DP800, and DP1000 steels. However, there are differences between the other two models and the Johnson-Cook damage model; from the comparisons of the figures, the strain concentration using the Johnson-Cook model is distributed almost uniformly or homogeneously over all the ferrite surfaces of the samples at all stages of deformation.

Notably, the crack propagations of the simulation results conformed well with the experimental findings. Thus far, there are no reports defining crack initiation, void nucleation, void growth, and crack propagation by considering these failure models and defining crack imitations in the martensite grains, as has been done through the simulations in this study. During the fracture analysis, it was found that the onset of cracks occurred in the martensite grain, and nucleation occurred either along the plastic strain or near the cross-sectional area. Fracture initiation usually occurs within

martensite islands. Nucleation occurred in both the martensite and ferrite phases, with voids formed within the ferrite phase at the martensite boundary being more common according to the findings of the current study. Owing to the applied deformation, the voids elongated, generating microcracks. The fissures subsequently spread between the martensite islands or ferrite grains. The crack propagated through the martensite grains when no alternative channel was available for the fracture propagation.

Author's Contributions: Conceptualization (equal), Methodology (equal), Investigation (equal), Writing - original draft (equal), Writing - review & editing Serkan Toros, Labinot Topilla, Funding acquisition, (equal), Resources, (equal).

Editor: Marco L. Bittencourt

References

- Çavuşoğlu, O., Toros, S., & Gürün, H. (2019). Microstructure based modelling of stress–strain relationship on dual phase steels. *Ironmaking and Steelmaking*, 46(4), 313–319. <https://doi.org/10.1080/03019233.2017.1371959>
- de Geus, T. W. J., Peerlings, R. H. J., & Geers, M. G. D. (2016). Competing damage mechanisms in a two-phase microstructure: How microstructure and loading conditions determine the onset of fracture. *International Journal of Solids and Structures*, 97_98, 687–698. <https://doi.org/10.1016/j.ijsolstr.2016.03.029>
- Feucht, M., Sun, D.-Z., Erhart, T., & Frank, T. (2006). Recent development and applications of the Gurson model. *LS-DYNA Anwenderforum*.
- Ghadbeigi, H., Pinna, C., & Celotto, S. (2013). Failure mechanisms in DP600 steel: Initiation, evolution and fracture. *Materials Science and Engineering A*, 588, 420–431. <https://doi.org/10.1016/j.msea.2013.09.048>
- Gurson, A.L. (1977). Continuum Theory of Ductile Rupture by Void Nucleation and Growth. Part I. Yield Criteria and Flow Rules for Porous Ductile Materials, *J. Eng. Mater. Technol. Trans.*, 99(1), p 2–15
- Horstemeyer, M. F., Ramaswamy, S., & Negrete, M. (2003). Using a micromechanical finite element parametric study to motivate a phenomenological macroscale model for void/crack nucleation in aluminum with a hard second phase. *Mechanics of Materials*, 35(7), 675–687. [https://doi.org/10.1016/S0167-6636\(02\)00165-5](https://doi.org/10.1016/S0167-6636(02)00165-5)
- Johnson, G. R., & Cook, W. H. (1983). A constitutive model and data from metals subjected to large strains, high strain rates and high temperatures. *Proc. 7th Int. Symp. on Ballistics, The Hague, Netherlands*.
- Johnson G.R., and Cook, W.H. (1985) Fracture Characteristics of Three Metals Subjected to Various Strains, Strain Rates, Temp. *Press. Eng. Fract. Mech.*, 21(1), p 31–48
- Katani, S., Ziaei-Rad, S., Nouri, N., Saeidi, N., Kadkhodapour, J., Torabian, N., & Schmauder, S. (2013). Microstructure Modelling of Dual-Phase Steel Using SEM Micrographs and Voronoi Polycrystal Models. *Metallography, Microstructure, and Analysis*, 2(3), 156–169. <https://doi.org/10.1007/s13632-013-0075-7>
- Lassance, D., Scheyvaerts, F., & Pardoën, T. (2006). No Title Growth and coalescence of penny-shaped voids in metallic alloys. *Engineering Fracture Mechanics*, 73, 1009–1.
- Li, S., Guo, C., Hao, L., Kang, Y., & An, Y. (2019). Microstructure-Based Modeling of Mechanical Properties and Deformation Behavior of DP600 Dual Phase Steel. *Steel Research International*, 90(12), 1–10. <https://doi.org/10.1002/srin.201900311>
- LS-DYNA® KEYWORD USER'S MANUAL VOLUME II Material Models LIVERMORE SOFTWARE TECHNOLOGY CORPORATION (LSTC). (2012). www.lstc.com
- Paul, S. K. (2013). Real microstructure based micromechanical model to simulate microstructural level deformation behavior and failure initiation in DP 590 steel. *Materials and Design*, 44, 397–406. <https://doi.org/10.1016/j.matdes.2012.08.023>
- Pickett, A. K., Pyttel, T., Payen, F., Lauro, F., Petrinic, N., Werner, H., & Christlein, J. (2004). Failure prediction for advanced crashworthiness of transportation vehicles. *International Journal of Impact Engineering*. <https://doi.org/10.1016/j.ijimpeng.2004.04.004>
- Ramazani, A., Schwedt, A., Aretz, A., Prah, U., & Bleck, W. (2013). Characterization and modelling of failure initiation in DP steel. *Computational Materials Science*, 75, 35–44. <https://doi.org/10.1016/j.commatsci.2013.04.001>

- Rice, J.R. Tracey, D.M. (1969). On the ductile enlargement of voids in triaxial stress fields, *J. Mech. Phys. Solids* 35; 201e217.
- Ruiz-Andresa, M., Condea, A., De Damboreneaa, J., & Garciaa, I. (2015). Microstructural and micromechanical effects of cold roll-forming on high strength dual phase steels. *Materials Research*, 18(4), 843–852. <https://doi.org/10.1590/1516-1439.000314>
- Rodriguez, R.-M., Gutierrez I. (2003). Unified formulation to predict the tensile curves of steels with different microstructures. *Mater Sci Forum*;426– 432:4525–30.
- Sirinakorn, T., Wongwiset, S., & Uthaisangskul, V. (2014). A study of local deformation and damage of dual phase steel. *Materials and Design*, 64, 729–742. <https://doi.org/10.1016/j.matdes.2014.08.009>
- Sodjit, S., & Uthaisangskul, V. (2012). A micromechanical flow curve model for dual phase steels. *Journal of Metals, Materials and Minerals*, 22(1), 87–97. <http://ojs.materialsconnex.com/index.php/jmmm/article/view/27>
- Szewczyk. A.F., and I. G. M. T. (1982). A study of the deformation and fracture of a dual phase steel.
- Toda, H., Takijiri, A., Azuma, M., Yabu, S., Hayashi, K., Seo, D., Kobayashi, M., Hirayama, K., Takeuchi, A., & Uesugi, K. (2017). Damage micromechanisms in dual-phase steel investigated with combined phase- and absorption-contrast tomography. *Acta Materialia*, 126, 401–412. <https://doi.org/10.1016/j.actamat.2017.01.010>
- Wu-rong, W., Chang-wei, H., Zhong-hua, Z., & Xi-cheng, W. (2011). The limit drawing ratio and formability prediction of advanced high strength dual-phase steels. *Materials and Design*, 32(6), 3320–3327. <https://doi.org/10.1016/j.matdes.2011.02.021>
- Yang, L., & Xing, Y. (n.d.). Experimental study on fatigue properties of Q420C steel welded joints at room temperature. 19(1), 1–15.
- Zhou, J., Gokhale, A. M., Gurumurthy, A., & Bhat, S. P. (2015). Realistic microstructural RVE-based simulations of stress-strain behavior of a dual-phase steel having high martensite volume fraction. *Materials Science and Engineering A*, 630, 107–115. <https://doi.org/10.1016/j.msea.2015.02.017>